CHEMISTRY OF MATERIALS

pubs.acs.org/cm

Article

Exploring the Thermoelectric Potential of MgB_4: Electronic Band Structure, Transport Properties, and Defect Chemistry

Sabrine Hachmioune, Alex M. Ganose, Michael B. Sullivan, and David O. Scanlon*

Cite This: *Chem. Mater.* 2024, 36, 6062−6073

Read Online

ACCESS | Metrics & More | Article Recommendations | Supporting Information

ABSTRACT: The demand for efficient and lightweight thermoelectric materials has surged due to their applications in electronics, wearable technology, and the aerospace industry. Conventional materials contain heavy, rare, and/or toxic elements, making them unsustainable for the future. This work presents a study of MgB_4, a material that has not been studied as a thermoelectric material. We use advanced computational chemistry techniques, combining electronic structure calculations, lattice dynamics, and full defect chemistry analysis, to predict the thermoelectric figure of merit, ZT, across a range of carrier concentrations and temperatures in the theoretical p-type and n-type systems. The study suggests that p-type MgB_4 is comparable to previously discovered Mg-based thermoelectrics under high-temperature conditions with a ZT of 0.47 at 1200 K. We also show that Ba-alloying up to 10% is a possible route toward improving thermoelectric performance as it increases the ZT to 0.66.

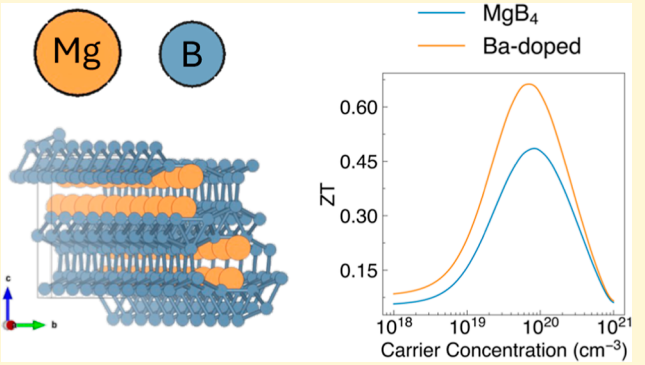

INTRODUCTION

Up to 50% of energy is wasted in the form of heat, most of which comes from industrial processes such as combustion.[1] The energy loss results in wasted resources and the need for excess fossil fuels to be burnt, contributing to global warming. Therefore, reducing the amount of wasted heat can help maximize energy efficiency, reduce costs, and minimize damage to the environment.[2]

Thermoelectric generators (TEGs) are a viable option to recover this wasted heat as they can be used in automobiles, furnaces, and industrial chimneys and have been shown to improve the combustion efficiency by up to 24%.[3,4] TEGs can also be used for power generation in industries such as aviation and aerospace or for biomedical applications such as medical devices.[5−7] However, for these applications, lightweight materials are required, and existing materials are limited by their toxicity, availability, and cost.

The thermoelectric efficiency is given by the thermoelectric figure of merit, ZT

$$\mathrm{ZT} = \frac{S^2\sigma T}{\kappa_l + \kappa_e} \quad (1)$$

where S is the Seebeck coefficient, σ is the electrical conductivity, T is the temperature, and κ_l and κ_e are the lattice and electronic thermal conductivity, respectively. Together, κ_l and κ_e make up the total thermal conductivity, κ ($\kappa_l + \kappa_e = \kappa$). The Seebeck coefficient and electrical conductivity terms ($S^2\sigma$) are referred to as the power factor (PF). Common thermoelectrics including PbTe and Bi_2Te_3 have ZT values of 1.40 at 873 K and 0.60 at 300 K, respectively.[8,9] These well-performing materials contain toxic elements such as lead or rare elements like tellurium making them unsustainable, hence the need for new viable alternatives.

A common criterion when searching for thermoelectric (TE) materials is the presence of heavy elements (densities between 6.5 and 8 g cm^{-3}) as they will tend to have lower lattice thermal conductivities; however, this makes them unfavorable for lightweight applications such as in deep space and wearable electronics.[10] Therefore, there is a need to discover novel lightweight materials that can function as thermoelectric semiconductors.[11]

Magnesium-based thermoelectric materials are an alternative to existing materials as they are eco-friendly, earth-abundant, and lightweight (density ∼ 2 g cm^{-3}).[12] Lightweight materials also have applications in portable electronics and wearable devices.[11,12] Existing Mg-based TEs include n-type Mg_2Si, p-type MgAgSb, and n-type Mg_3Sb_2. The former, Mg_2Si, has been shown to achieve a promising ZT of 1 with Ge and Sn alloying, while α-MgAgSb has reported a ZT of 0.56 at 500

Received: March 4, 2024
Revised: May 17, 2024
Accepted: May 20, 2024
Published: June 4, 2024

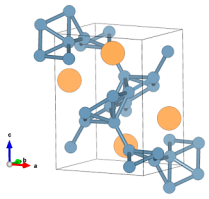

(a) Primitive unit cell of MgB_4 containing 20 atoms.

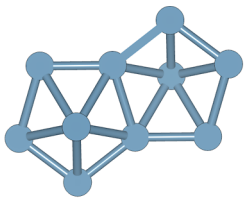

(b) B_6-pentagonal clusters that make up the boron-framework.

Figure 1. Figures made using VESTA.[21] Mg atoms shown in orange and B atoms shown in blue. (a) Primitive unit cell of MgB_4 containing 20 atoms. (b) B_6-pentagonal clusters that make up the boron framework.

K.[12,13] Mg_3Sb_2 has an ultralow lattice thermal conductivity, and upon doping with Na or Ag, it has been shown to achieve ZTs of up to 0.60 and 0.51 at 773 and 725 K, respectively.[14,15] This system is intrinsically p-type; however, it can only achieve low carrier concentrations in the order of 10^{17}, limiting its thermoelectric performance.[15]

In this work, we calculate the thermoelectric and defect properties of MgB_4, an experimentally known, Mg-based semiconductor and derivative of MgB_2.[16] MgB_2 has been studied for its unique superconducting properties that are possibly a result of its layered structure of alternating Mg and B layers, whereas MgB_4 contains a network of pentagonal B_6-clusters with Mg positioned between them (shown in Figures 1, S1 and S2).

The difference in electronic properties between the two systems is likely a result of the difference in structure. Esfahani et al. report that at 31 GPa, the semiconducting *Pnma* phase breaks down into a metallic *C*2/*m* phase, which can act as a potential superconductor.[17] This structure is described as having graphene-like layers of boron intercalated with magnesium atoms, while the *Pnma* phase is made up of those B_6-clusters mentioned above, which extend along the *b*-axis, forming a boron-framework of channels containing magnesium.

MgB_4 has been synthesized via solid-state reaction of elemental powders followed by high-temperature sintering and has been used as a precursor for the synthesis of MgB_2.[18]

We use first-principles hybrid density functional theory (DFT) and lattice dynamics.[19] Previous theoretical works predicted a bandgap of 1.6 eV and suggested that the electronic states near the Fermi level were localized, predicting one-dimensional electrical conductivity.[20]

MgB_4 crystallizes in a complex (*Pnma*) crystal structure, which should yield low lattice thermal conductivity. As with other ideal thermoelectric candidates, the transport properties in MgB_4 can be manipulated by doping or alloying on the Mg site with the added benefit of also being lightweight.

COMPUTATIONAL METHODS

DFT calculations were carried out using the Vienna ab initio simulation package[22−25] and the projector augmented-wave[26,27] pseudopotential method to describe the interactions between core and valence electrons. A plane-wave energy cutoff and Γ-centered *k*-point mesh of 400 eV and 3 × 4 × 2 were used, respectively. Both parameters were converged to within 1 meV $atom^{-1}$.

Electronic structure and transport property calculations used the Heyd−Scuseria−Ernzerhof hybrid exchange−correlation density functional (HSE06).[19] HSE06 contains 25% screened Hartree−Fock exchange, more accurately describes the band structure and avoids the self-interaction problem found in Generalized Gradient Approximation (GGA) functionals.[28] The revised GGA functional, Perdew−Burke−Ernzerhof (PBEsol),[29] was used for structural properties and lattice dynamics calculations as it is able to replicate lattice parameters at lower computational cost.[30−35]

The 20-atom primitive unit cell of MgB_4 (Figure 1a) was optimized using the PBEsol and HSE06 functionals to a force convergence criterion of 0.01 eV $Å^{-1}$ with an energy cutoff of 520 eV to account for Pulay stress.[36]

Band alignment calculations were carried out using the HSE06 functional on an optimized conventional unit cell as the bulk, and a slab (001) generated using the Surfaxe code was used as the surface.[37]

Thermoelectric Properties. The linearized Boltzmann transport equation was solved using the AMSET code to calculate the Seebeck coefficient, electrical conductivity, electronic thermal conductivity, and mobility.[38] AMSET uses the momentum relaxation-time approximation to calculate the contributions from acoustic deformation potential (ADP), ionized impurities (IMP), polar-optical phonons (POP), and piezoelectricity (PIE) scattering mechanisms. AMSET also allows for the effect of nanostructuring to be simulated.

The unit cell was tightly relaxed to a force convergence criterion of 0.0005 eV $Å^{-1}$ using HSE06, and the deformation potential and wave function of MgB_4 were extracted using the AMSET code. A dense *k*-point mesh of 12 × 15 × 9 was used for the latter. This mesh was interpolated to 37 × 45 × 27 for transport calculations. The optical dielectric constant was calculated using the HSE06 functional and a converged number of bands (60).

The elastic constant, ionic dielectric constant, piezoelectric coefficients, and POP frequency were computed using density functional perturbation theory and finite differences. A tightly relaxed cell was used with a plane-wave energy cutoff and *k*-point mesh converged to $\Delta\varepsilon_0 < 0.1$. The PBEsol functional was used to reduce the computational cost along with the converged *k*-point mesh.

To determine the vibrational properties, the primitive unit cell was optimized to a tight force convergence criterion of 0.0001 eV $Å^{-1}$, using the PBEsol functional. The phonon dispersions were calculated using the Phonopy code, which uses the supercell and finite displacement approach to calculate second-order force constants.[39,40] A 480-atom, 4 × 3 × 2 supercell was used with Γ-only 1 × 1 × 1 *k*-points.

Third-order force constants were calculated by direct solution of the phonon Boltzmann equation using the Phono3py code to determine the lattice thermal conductivity.[40,41] The same functional and optimized cell was used on a smaller 160-atom, 2 × 2 × 2 supercell, with 2 × 2 × 1 *k*-points. The lattice thermal conductivity was converged to an 18 × 14 × 11 *q*-point mesh. Phono3py was also used to simulate the effect of nanostructuring and alloy scattering on the lattice thermal conductivity.

Figures were plotted using the sumo and ThermoParser packages.[42,43]

Defects. The optimized 20-atom primitive cell was used to make a 120-atom supercell to host the defects using the TDEP code and the following supercell matrix[44]

$$\begin{Bmatrix} 1 & 2 & 0 \\ -1 & 1 & -1 \\ -1 & 1 & 1 \end{Bmatrix}$$

The supercell was 10.3 × 10.2 × 10.2 Å to minimize interactions between defects in neighboring supercells.[45]

https://doi.org/10.1021/acs.chemmater.4c00584
Chem. Mater. 2024, 36, 6062−6073

The 5 stable competing phases in the Mg−B phase space (Mg, B, MgB_2, MgB_4, and MgB_7) were taken from the Materials Project[46] and relaxed using their converged *k*-points, 400 eV energy cutoff, and the HSE06 functional. These phases were used to calculate the chemical potentials and then plotted using the CPLAP package.[47]

The doped package[48] was used to generate defect supercells containing vacancies (31), antisites (31), and interstitials (168). These defects were also calculated in all the possible charge states totaling to 236 defect supercells.

The cells were relaxed using HSE06, 400 eV cutoff, and 2 × 2 × 2 Γ-centered *k*-point mesh. The converged DFT energies were used to calculate the formation energy of each defect and plot transition level diagrams with the doped code. The ShakeNBreak package[49−51] was then used to introduce bond distortions to each defect cell at 10, 30, and 60% to find lower energy ground-state structures not captured by the initial relaxations.

The self-consistent Fermi level and predicted defect concentrations were calculated using the py-sc-fermi package.[52,53]

RESULTS AND DISCUSSION

Geometry Optimization. MgB_4 crystallizes in the orthorhombic space group, *Pnma* with the following experimental lattice parameters; a = 5.46, b = 4.43, c = 7.47 Å, $\alpha = \beta = \gamma = 90°$.[54] Each B atom is bonded to four other B atoms forming a connected framework throughout the lattice.

The boron atoms are bonded in B_6 pentagonal clusters, forming layers throughout the *a*-axis (shown in Supporting Information 1). The Mg atoms sit between the layers in empty channels. These channels are more clearly observed along the *b*-axis (Figure 2), where the Mg atoms are enclosed in the

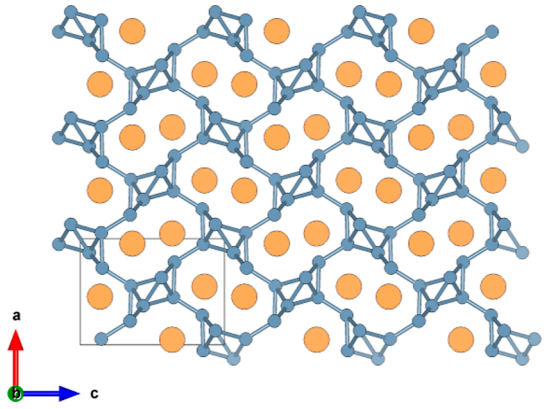

Figure 2. View from the *b*-axis perspective of MgB_4 made from the unit cell, repeated 3 × 3 × 3 in each direction. The figure was made using VESTA.[21]

boron framework. By comparison, along the *c*-axis, the Mg atoms are interpenetrated between the boron layers (shown in Supporting Information 2).

The hybrid-DFT functional, HSE06, and the GGA functional, PBEsol, were used to optimize the primitive cell with the calculated lattice parameters, as shown in Table 1. The lattice parameters predicted by the PBEsol functional were in agreement with the experimentally reported values (±1%); therefore, this functional was used to calculate structural properties such as the phonon dispersions and elastic constants.

Table 1. Calculated Lattice Parameters of the Primitive MgB_4 Unit Cell Using the HSE06 and PBEsol Functionals[a]

	a/Å (%)	b/Å (%)	c/Å (%)	α/°
experimental	5.46	4.43	7.47	90.0
HSE06	5.19 (−5)	4.36 (−1.6)	7.45 (−0.3)	90.0
PBEsol	5.44 (−0.3)	4.38 (−1.1)	7.42 (−0.7)	90.0

[a]Percentage differences are shown in brackets.

The HSE06 functional underestimates the lattice parameters in the *a*-direction by 5%, which may be due to thermal expansion, which was shown by Yang et al. to have a considerable effect in light materials.[55]

Electronic Structure. The hybrid-HSE06 functional was used to calculate the electronic properties of MgB_4 with the optimized HSE06 structure. The bandgaps of the system were calculated to give a direct bandgap of 1.32 eV and an indirect bandgap of 0.71 eV. Previous studies reported a single bandgap of 1.60 eV using the LDA functional.[20] By comparison, the PBEsol functional predicted smaller direct and indirect bandgaps of 0.75 and 0.34 eV, respectively. This is expected, as PBEsol is known to underestimate the bandgap.[28]

The density of states (DOS) (Figure 3) shows that both the valence and conduction bands are predominantly made up of

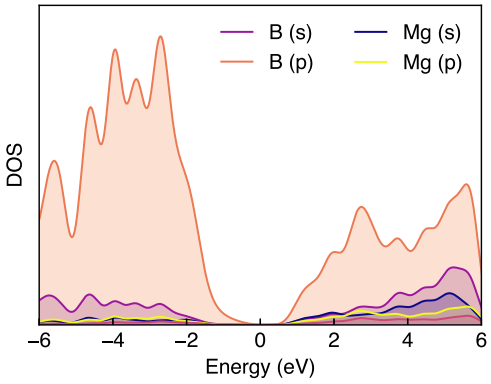

Figure 3. DOS of MgB_4 calculated using the HSE06 functional showing the atoms and respective states that contribute to the total DOS. The figure was plotted using sumo.[42]

boron p-states, followed by boron s-states, suggesting conduction is mostly occurring throughout the boron-framework. This was also observed in previous studies, with the states near the Fermi level being composed of B 2p states.[56] Conductivity along the boron-framework was reported by Sato et al., who predicted one-dimensional electrical conductivity as a result of the B_6 cluster chains.[54]

The electronic band structure shown in Figure 4 can be used to indicate what the electronic properties and behavior of the material will be. The band edges are shown at the valence band maximum (VBM) and conduction band minimum (CBM). The VBM is at the Γ point, whereas in the CBM, it is positioned between *Z* and *T*. The effective mass is inversely proportional to the curvature of the bands, so steep and disperse bands indicate low effective masses, while flat bands indicate high effective masses. The effective masses in this system are given in Table 2.

Disperse bands with light charge carriers contribute to good electrical conductivity; however, flat heavy bands improve the Seebeck coefficient. In addition, the VBM is composed of a single band with relatively low effective masses, whereas the CBM is doubly degenerate with higher effective masses. Degeneracy has been shown to improve thermoelectric performance by providing more states near the Fermi level.[58]

https://doi.org/10.1021/acs.chemmater.4c00584
Chem. Mater. 2024, 36, 6062−6073

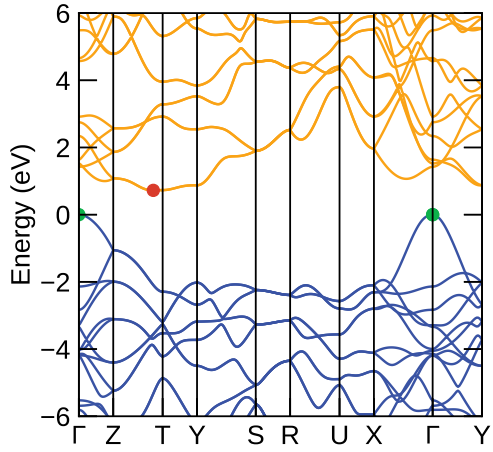

Figure 4. Electronic band structure of MgB_4 calculated using the HSE06 functional and plotted along the *k*-point path derived from the Bradley−Cracknell formalism.[57] The valence bands are shown by blue lines and the conduction bands are shown by orange lines. The band edges making up the bandgap are shown by the green (VBM) and red (CBM) markers. The figure was made using sumo.[42]

Table 2. Calculated Hole and Electron Effective Masses Using the HSE06 Functional[a]

band	direction	m_h^* (m_e)	band	direction	m_e^* (m_e)
VBM	Γ−*X*	0.418	CBM	pCBM−T	2.734
	Γ−*Y*	0.528		pCBM−Z	1.188
	Γ−*Z*	0.228			

[a]These values were extracted from the band structure calculation using the sumo code.[42] Position of the conduction band minimum = [−0.41, 0.00, 0.50].

In addition to flat bands and degeneracy, band extrema (VBM/CBM) being positioned off-gamma at nonhigh-symmetry points also improves thermoelectricity as these points exist in multiple points of reciprocal space, having the same effect as band degeneracy.[59] The n-type system shows double band degeneracy at [−0.41, 0.00, 0.50] *k*-points, suggesting it will have a greater Seebeck coefficient due to flat bands, band degeneracy, and the CBM being positioned off-gamma.

The effective masses are inversely related to the carrier mobility. This relationship suggests that the hole carrier mobility will be greater than the electron carrier mobility due to the lower effective mass in the VBM. The effective masses also suggest that hole transport will be greatest in the Γ−*Z* direction due to it having the lowest effective mass. This direction corresponds to the *b*-axis view shown in Figure 2, where the Mg atoms are positioned in open channels. The transport in the Γ−*X* and Γ−*Y* directions will be comparable.

The band alignment was calculated using the core and vacuum energies from the surface-slab (001) made using the Surfaxe code.[37] Figure 5 shows the band alignment of MgB_4 alongside that of well-studied thermoelectrics, PbTe and SnTe. The ionization potential of MgB_4 is relatively large (5.1 eV) and greater than that of PbTe and SnTe, meaning it is likely to be less p-type than these systems. The electron affinity of the system (4.3 eV) is lower than that of PbTe (4.6 eV),[60] a system that can act as a bipolar semiconductor, but greater than that of SnTe (4.1 eV).[61]

Lattice Dynamics. The phonon dispersions for a 480-atom MgB_4 supercell are shown in Figure 6. The calculated dispersions show no imaginary modes, suggesting the system

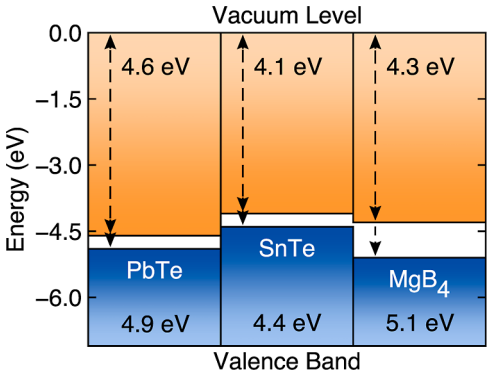

Figure 5. Band alignment of MgB_4 calculated using the HSE06 functional and compared to that of PbTe[60] and SnTe.[61] This figure was plotted with bapt.[62]

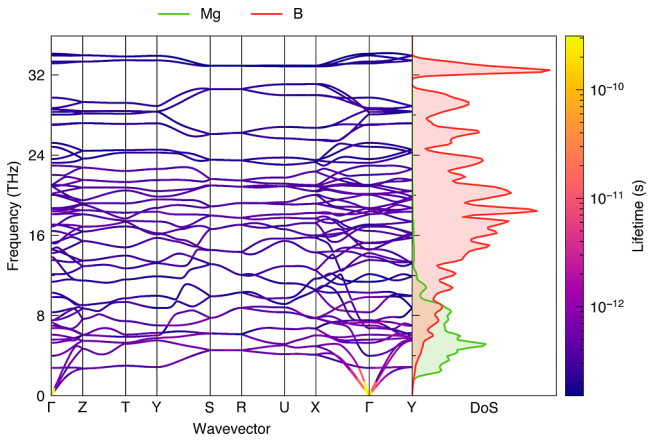

Figure 6. Phonon band structure of MgB_4 calculated using the PBEsol functional and Phonopy package on a 480-atom, 4 × 3 × 2 supercell.[39] The figure was plotted along the *k*-point path derived from the Bradley−Cracknell formalism[57] using ThermoParser.[43] The phonon lifetimes are shown by the color bar and were calculated using the Phono3py code.[39,40]

is dynamically stable. The steep acoustic modes can be seen branching out from 0 up to 6 THz before flattening out. A single optic mode can also be seen in this 0 to 6 THz region. Above the acoustic modes, there are flatter optic modes which go as high as 34.2 THz.

The projected density of states shows that the Mg atoms mostly contribute to the acoustic modes, whereas the B atoms contribute to the optic modes. Steep bands indicate high group velocity and, therefore, a high lattice thermal conductivity. This suggests that alloying on the Mg site would have the greatest effect on the lattice thermal conductivity.

Some avoided crossings are observed between the acoustic and optic modes in the Γ−*X* direction around 6 THz and again in the *Y*−*S* direction from 6 to 18 THz. Avoided crossings suggest that there are channels for the phonons to scatter into, reducing the group velocity and so the lattice thermal conductivity. They can also be indicative of symmetry-disallowed transitions or rattler species in the system, in this case, the Mg atoms sitting in the boron framework.[63]

The calculated lattice thermal conductivity, κ_l (given in Figure 7), is shown to decrease across the temperature range (300−1200 K) in all directions. The average κ_l at 300 K is 11.6 W m^{-1} K^{-1}; however, from the figure, there is notable anisotropy between the *x* direction (18.6 W m^{-1} K^{-1}) and *y*/*z*-

https://doi.org/10.1021/acs.chemmater.4c00584
Chem. Mater. 2024, 36, 6062−6073

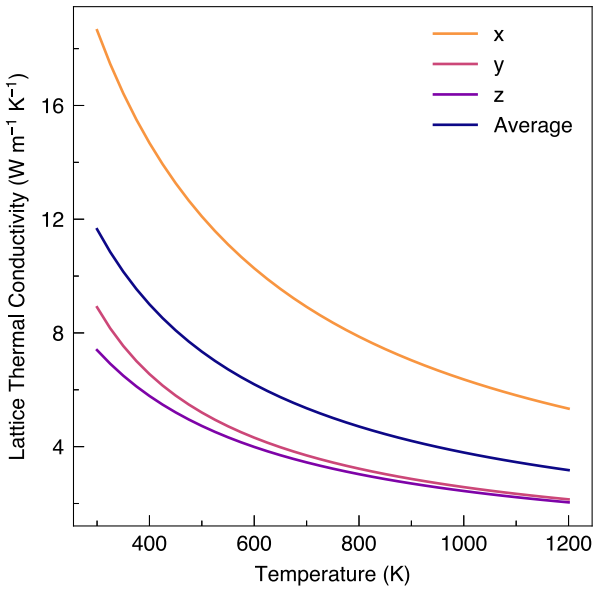

Figure 7. Calculated lattice thermal conductivity (κ_l) of MgB_4 as a function of temperature up to 1200 K in the *x*, *y*, *z*, and average directions. The κ_l was calculated using the Phono3py code and plotted using ThermoParser.[39,40]

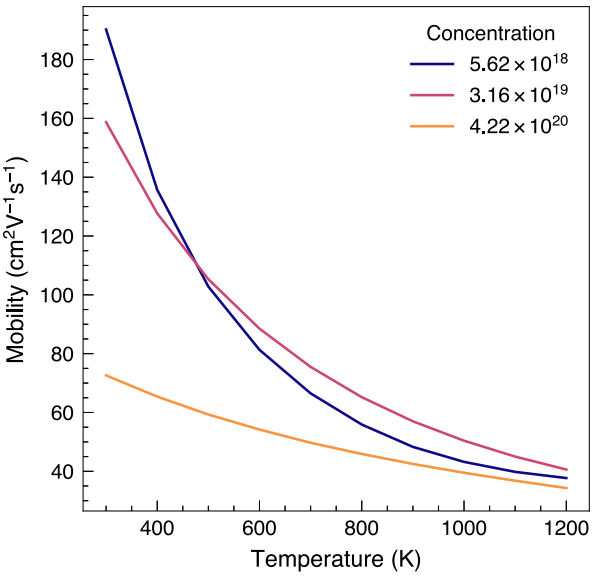

Figure 8. Mobility of the p-type system at three carrier concentrations across the full temperature range.

directions (8.9/7.4 W m^{-1} K^{-1}). Note, the *x*, *y*, and *z* directions correspond to a, b, and c, respectively, as shown in Figures 1 and 2.

At high temperatures up to 1200 K, the difference between the *y* and *z* directions (2.2/2.0 W m^{-1} K^{-1}) is less pronounced, but the thermal conductivity in the *x* direction is still more than double (5.3 W m^{-1} K^{-1}), giving an average lattice thermal conductivity of 3.2 W m^{-1} K^{-1}.

Figure 6 also shows the phonon lifetimes per band. The acoustic modes in the Γ−*X* and Γ−*Y* directions below 5 THz have the greatest phonon lifetimes, likely contributing the most to the lattice thermal conductivity. Nevertheless, the average value at room temperature is comparable to that of existing thermoelectrics such as $SrTiO_3$ (12 W m^{-1} K^{-1}).[64,65]

Transport Properties. The electronic transport properties were calculated from 1 × 10^{18} to 1 × 10^{21} and 1 × 10^{19} to 1 × 10^{22} cm^{-3} for the p-type and n-type systems, respectively, in the range of 300−1200 K.

The mobility at room temperature in the p-type system (233.7 cm^2 V^{-1} s^{-1} at 1 × 10^{18} cm^{-3} carriers) is greater than that in other well-known thermoelectrics such as SnTe (178 cm^2 V^{-1} s^{-1}) and $AgSbTe_2$ (58.5 cm^2 V^{-1} s^{-1}),[66] which has a ZT of 1.59 at 673 K.[67] Figures 8 and S9 show the relationship between the mobility, temperature, and concentration. In both systems, the mobility decreases with an increase in temperature, especially at low carrier concentrations, suggesting the system has metallic-like behavior where increased thermal motion increases scattering and decreases conductivity.

The mobility (given in Table 3) generally decreases with an increase in carrier concentration from 233.7 cm^2 V^{-1} s^{-1} (1.00 × 10^{18} cm^{-3}) to 44.6 cm^2 V^{-1} s^{-1} (1.00 × 10^{21} cm^{-3}). However, at 3.16 × 10^{19} and 7.50 × 10^{20} cm^{-3} in the p-type and n-type systems, respectively, the mobility above ∼500 K is greater than at lower concentrations.

The scattering rates for the p-type and n-type systems are shown in Figures 9 and S10. A fixed temperature of 1200 K and carrier concentrations of 7.50 × 10^{19} and 3.16 × 10^{20} cm^{-3} were used for the p-type and n-type systems, respectively. POP scattering dominates at constant carrier concentration and temperature in the p-type system with the exception of low temperatures where ionized impurity (IMP) scattering is more dominant. Throughout the whole temperature and carrier concentration range, ADP scattering makes the lowest contribution.

Table 3. Calculated Mobility, μ, for the p-type (7.50 × 10^{19} cm^{-3}) and n-type (3.16 × 10^{20} cm^{-3}) Systems at 300, 700, and 1200 K

	T/K	μ/cm^2 V s
p-type	300	127.0
	700	72.5
	1200	42.5
n-type	300	47.6
	700	31.0
	1200	20.2

In the n-type system, IMP is the most dominant scattering mechanism. At constant temperature, the contributions from POP decrease and are overtaken by IMP at 1 × 10^{20} cm^{-3}. Similar to the p-type system, ADP contributes the least.

The electrical conductivity, σ, Seebeck coefficient, *S*, electronic thermal conductivity, κ_e, and PF are shown in Figures 10 and S11.

The κ_e for this system at 700 K are 1.57 W m^{-1} K^{-1} (n-type) and 0.81 W m^{-1} K^{-1} (p-type). These values are lower than in other systems like SnTe (2.18 W m^{-1} K^{-1}).[68] Relative to the lattice thermal conductivity, κ_l, the electronic component does not contribute a lot at low temperatures; however, as the κ_l decreases, the contribution of the κ_e increases to 27/38% from 8/12% (p-type/n-type).

The Seebeck coefficient is more complex and depends on factors such as the number of charge carriers and number of states near the Fermi level. A large carrier concentration has a negative effect on the Seebeck coefficient, as shown by the following equations

https://doi.org/10.1021/acs.chemmater.4c00584
Chem. Mater. 2024, 36, 6062−6073

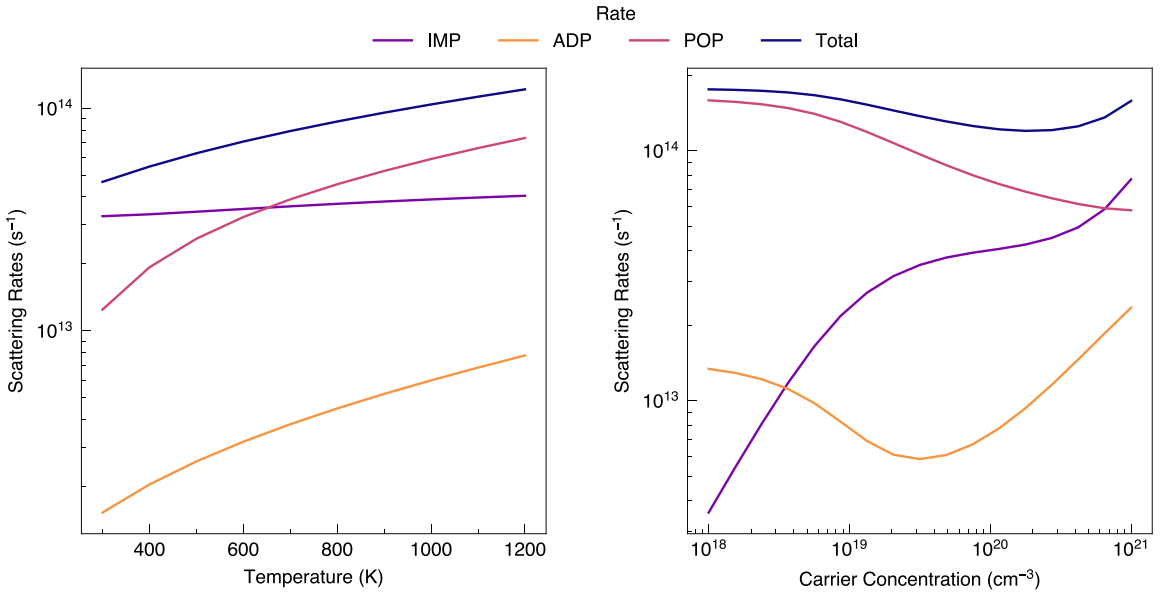

Figure 9. Scattering mechanisms in the p-type system at constant concentration (7.50×10^{19} cm^{-3}) (left) and constant temperature (1200 K) (right).

$$S = \frac{C_{el}}{q} \approx \left(\frac{k_B}{e}\right)\frac{E_g}{k_B T} \tag{2}$$

where C_{el} is the electronic specific heat capacity, q is the charge of the carrier, k_B is the Boltzmann constant, e is the elementary charge of an electron, E_g is the bandgap, and T is the temperature, and

$$S = \frac{k_B}{e}\left[\ln\left(\frac{N}{n}\right) + 2.5 - r\right] \tag{3}$$

where N is the DOS near the Fermi level, n is carrier concentration, r is the scattering mechanism parameter, e is the electron charge, and k_B is the Boltzmann constant.[58]

The Seebeck coefficient at 700 K is -204 μV K^{-1} (n-type) and 125 μV K^{-1} (p-type); this is comparable to that of existing thermoelectric Bi_2Te_3, which has a value of -170 μV K^{-1} (n-type) and 160 μV K^{-1} (p-type).[66]

The results show that as the carrier concentration increases, the electrical conductivity also increases; however, overall conductivity decreases steadily across the temperature range. Conversely, the magnitude of the Seebeck coefficient decreases with increasing carrier concentration and increases with temperature until 800 K. At temperatures above 800 K and carrier concentrations $\sim 1 \times 10^{19}$ cm^{-3}, the magnitude of the Seebeck coefficient begins to decrease significantly.

The deviations at low carrier concentrations and high temperatures in both systems are a result of bipolar effects. This occurs when the temperature is high enough to excite charge carriers across the bandgap and reduce the Seebeck coefficient and electrical conductivity above a certain temperature.

The PF shown in Figures 10 and S11 can be used to determine the optimum carrier concentrations at various temperatures. The n-type system is easier to assess as 7.50×10^{20} cm^{-3} appears to dominate throughout the temperature range.

As for the p-type system, at low temperatures, PF peaks at 3.16×10^{19} cm^{-3}, followed by 7.50×10^{19} cm^{-3} at intermediate temperatures, and finally 1.78×10^{20} cm^{-3} at high temperatures. The effects of the electronic thermal conductivity would have to be factored in to determine when performance is optimized.

The difference between the p-type and n-type systems with respect to the scattering mechanisms is shown earlier in Figures 9 and S10. POP scattering occurs when atoms are displaced by optical vibrations in the lattice (optical phonon modes), whereas ionized impurity scattering occurs from the scattering of charge carriers. The differing contributions from these mechanisms may be responsible for the differing thermoelectric performance.

In addition, the CBM, which determines transport in the n-type system, is doubly degenerate (Table 2 and Figure 4), and band degeneracy has been shown to improve thermoelectric performance, which would explain the significant difference in conductivity between the n-type and p-type systems, as well as the greater Seebeck coefficients.[69,70]

Figure of Merit. The thermoelectric figure of merit, ZT, is given for the p-type (Figure 11) and n-type (Figure S12) systems. In both cases, the ZTs increase with temperature. The p-type system exhibits a ZT max of 0.48 at 1200 K and 7.50×10^{19} cm^{-3}, while the n-type system yields a much greater ZT of 1.57 at 1200 K and 3.16×10^{20} cm^{-3}.

The transport properties and predicted ZT for each system at their optimum carrier concentration and three temperature points are given in Table 4. At the same temperature, the n-type system has greater Seebeck coefficients and electrical conductivities relative to the p-type system at its respective optimum carrier concentration. As a result, the PF is greater in the n-type system relative to the p-type, and despite the greater electronic thermal conductivity, it yields greater ZTs.

Intrinsic Defects. The intrinsic defect chemistry was studied to determine whether the optimum carrier concentrations for the p-type and n-type systems can be achieved or whether the material is dopable. All the vacancies, antisites, and interstitials in the material were modeled using the doped python package,[48] and the true defect ground states were found using the ShakeNBreak code.[49−51]

https://doi.org/10.1021/acs.chemmater.4c00584
Chem. Mater. 2024, 36, 6062−6073

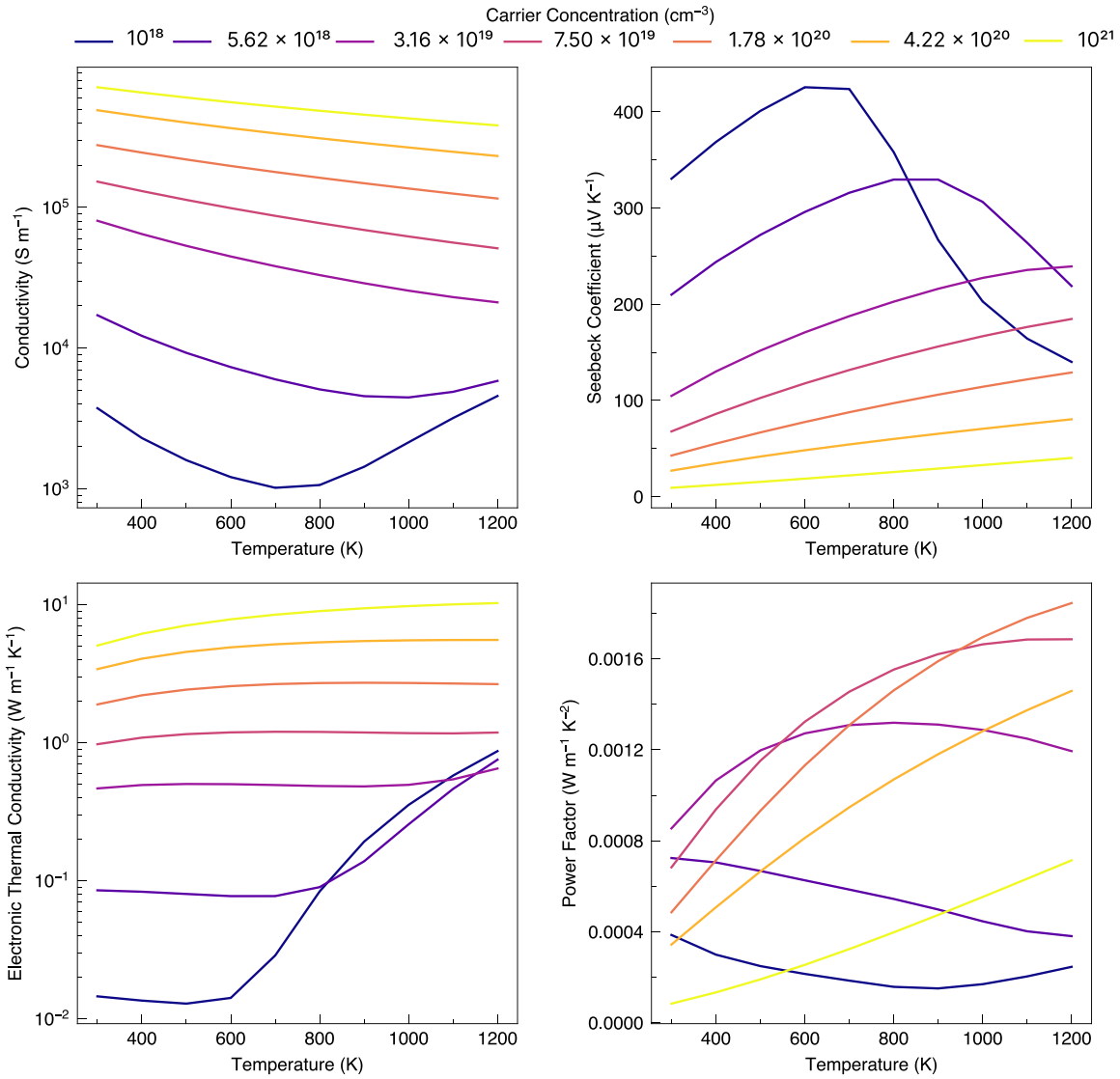

Figure 10. Transport properties of MgB_4 in the average direction, with p-type doping (positive charge carriers) calculated and plotted using AMSET. Transport properties include the electrical conductivity, Seebeck coefficient, electronic component of the thermal conductivity, and the PF ($S^2\sigma$).

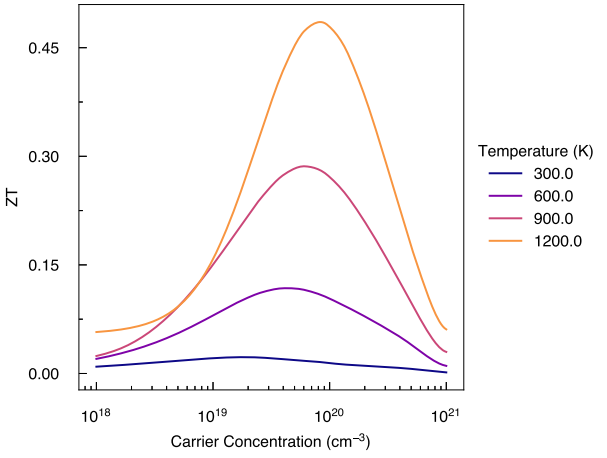

Figure 11. Thermoelectric figure of merit, ZT, for the p-type system at a constant concentration of 7.50 × 10^{19} cm^{-3} and four temperature points between 300 and 1200 K. The figure was plotted using ThermoParser.[43]

The thermodynamic stability region for MgB_4 is shown in Figure 12. The most p-type growth conditions are at the point where MgB_4 and MgB_7 cross over (Mg-poor/B-rich), and the n-type growth conditions are shown by the crossover between MgB_4 and MgB_2 (Mg-rich/B-poor).

Figure 13a,b shows the defect transition level diagrams for each condition. Under both conditions, the V_{Mg} defect is the most favored and prevents the system from being n-type doped, acting as a "killer" defect. This defect has a formation energy of 0.90 eV in the −2 charge state under Mg-poor conditions and 1.05 eV in Mg-rich conditions.

The next likely defect to form is the V_B defect in the −1 charge state, with formation energies between 3.20 and 4.36 eV depending on the site and conditions. The remaining intrinsic defects, Mg_B, B_{Mg}, Mg_i, and B_i, have formation energies greater than 4 eV, so they will likely be present in minute concentrations.

The predicted carrier concentrations at the Fermi level are 1.05 × 10^{20} and 1.60 × 10^{20} cm^{-3} under Mg-rich/B-poor and Mg-poor/B-rich conditions, respectively. These values are

https://doi.org/10.1021/acs.chemmater.4c00584
Chem. Mater. 2024, 36, 6062−6073

Table 4. Calculated Transport Properties and ZT for the p-Type (7.50×10^{19} cm^{-3}) and n-Type (3.16×10^{20} cm^{-3}) Systems at 300, 750, and 1200 K

	T/K	σ/S m^{-1}	S/V K^{-1}	κ_e/W m^{-1} K^{-1}	PF/μW m^{-1} K^{-2}	κ_l/W m^{-1} K^{-1}	ZT
p-type	300	153,000	68	0.98	0.68	11.6	0.02
	750	87,100	132	1.20	1.46	5.01	0.19
	1200	51,200	185	1.18	1.69	3.17	0.48
n-type	300	241,000	−123	1.63	3.64	11.6	0.10
	750	157,000	−216	2.15	7.17	5.01	0.77
	1200	102,000	−264	1.97	6.89	3.17	1.57

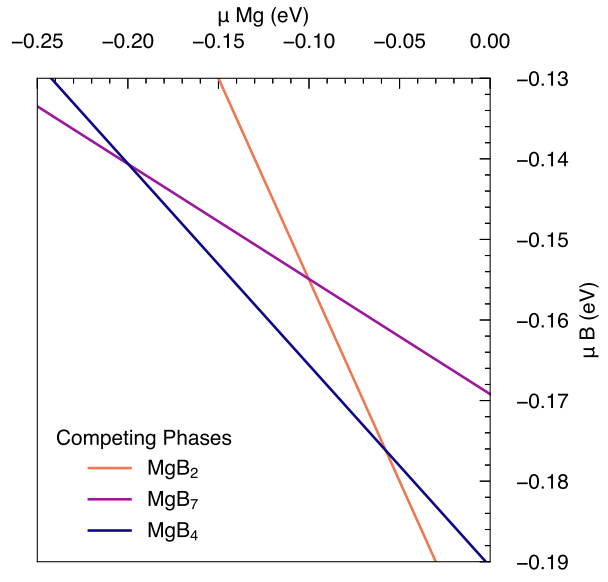

Figure 12. Chemical potential limits of the MgB_2−MgB_4−MgB_7 phase space.

greater than the predicted optimum of 7.50×10^{19} cm^{-3}; therefore, further p-type doping would not optimize the system. An n-type dopant such as Sc or Y could be investigated on the Mg site to increase the electron carrier concentration and reduce the overall number of carriers available for charge transport.

These results suggest that the system is most likely to be a degenerate p-type semiconductor and is not n-type dopable, meaning that the high ZTs predicted in the n-type system are not feasible.

Nanostructuring. Upon nanostructuring, the lattice thermal conductivities are significantly reduced by as much as 51% in the 15 nm system at 300 K. The average values are shown in Figure 14 as a function of temperature. This

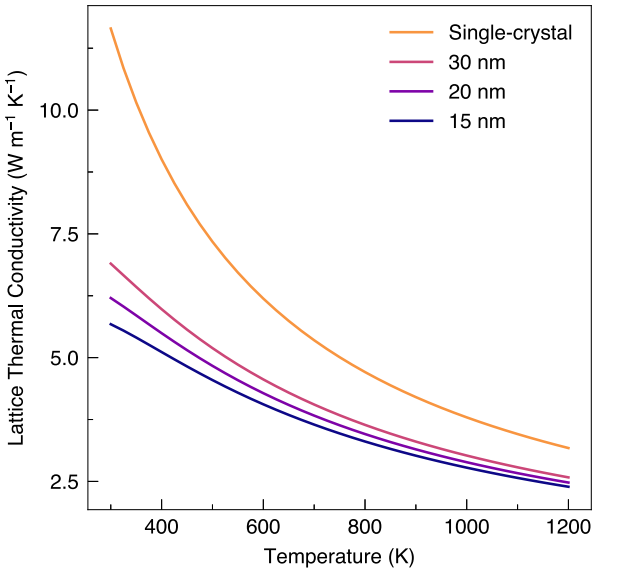

Figure 14. Nanostructured lattice thermal conductivity (κ_l) of MgB_4 at 15, 20, and 30 nm as a function of temperature up to 1200 K in the average direction. The κ_l was calculated using the Phono3py code and plotted using ThermoParser.[39,40,43]

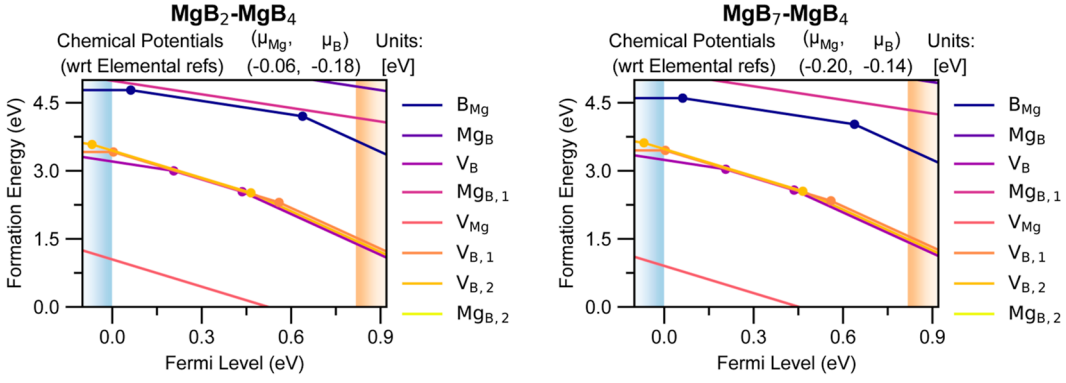

(a) Transition level diagram of the intrinsic defects in MgB_4 under Mg-rich/B-poor conditions.

(b) Transition level diagram of the intrinsic defects in MgB_4 under Mg-poor/B-rich conditions.

Figure 13. Figures made using the doped code.[48] (a) Transition level diagram of the intrinsic defects in MgB_4 under Mg-rich/B-poor conditions. (b) Transition level diagram of the intrinsic defects in MgB_4 under Mg-poor/B-rich conditions.

https://doi.org/10.1021/acs.chemmater.4c00584
Chem. Mater. 2024, 36, 6062−6073

Table 5. Transport Properties of the Single Crystal and 15 nm System at 7.50×10^{19} cm^{-3} Calculated Using AMSET and Phono3py

T/K	type	σ/S m^{-1}	S/V K^{-1}	κ_e/W m^{-1} K^{-1}	κ_l/W m^{-1} K^{-1}	μ/cm^2 V s	ZT
300	single crystal	153,000	68	0.98	11.60	127.0	0.016
	15/nm	88,600	61	0.56	5.67	73.8	0.015
1200	single crystal	51,200	185	1.18	3.17	42.5	0.480
	15/nm	39,200	180	0.90	2.39	32.5	0.440

reduction in lattice thermal conductivity suggests that nanostructuring may be a possible route toward optimizing the material's thermoelectric performance by reducing thermal transport. Although explicit nanostructuring of MgB_4 has not been shown, Pfefferle et al. showed success in synthesizing Mg_xB_y nanostructures with diameters of 3−5 nm.[71]

The effect of nanostructuring on the electronic transport properties was also investigated using the AMSET code by introducing mean free path scattering.

The transport properties of the 15 nm system are shown in Table 5 compared to those of the single crystal at 300 and 1200 K. The results show that at both low and high temperatures, the electrical conductivity, Seebeck coefficient, electronic thermal conductivity, and mobilities decrease relative to the single crystal. Combined with the reduction in lattice thermal conductivity, the ZTs of the nanostructured systems are comparable to the single crystal but not significantly improved (Figure 15). This is because the reduction in thermal conductivity is canceled out by the reduction in electrical conductivity.

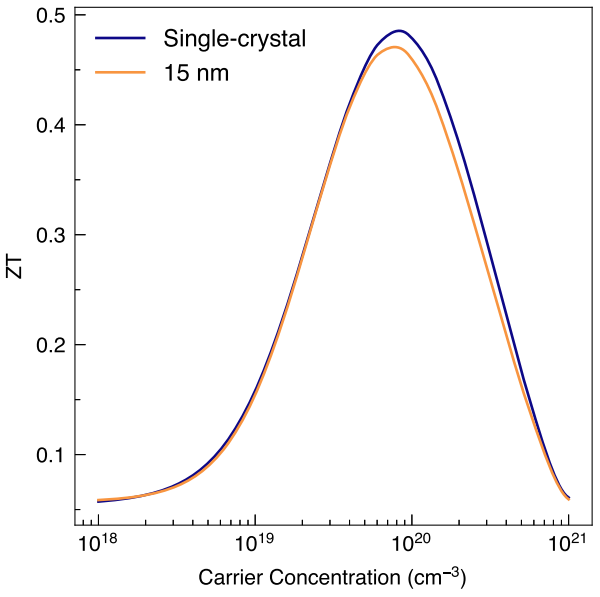

Figure 15. Thermoelectric figure of merit, ZT, of single-crystal MgB_4 and the 15 nm nanostructured system at 1200 K. The figure was plotted using ThermoParser.[43]

Alloy Scattering. Given the sensitivity of the electronic transport properties, another way of manipulating the lattice thermal conductivity is alloying the Mg site which contributes the most to the lattice thermal conductivity. Alloying up to 10% on this site with isovalent group 2 atoms (Ca, Sr, and Ba) was simulated using the Phono3py code.

The lattice thermal conductivity of the alloyed systems is shown in Figure 16. The greater the mass difference between

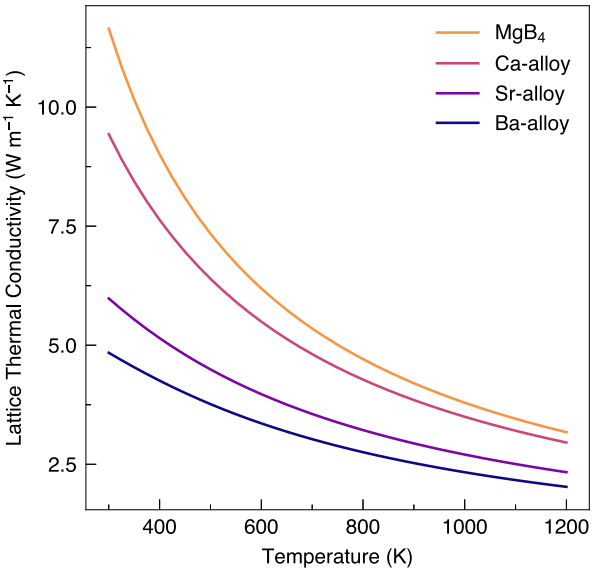

Figure 16. Lattice thermal conductivity of MgB_4, Ca-, Sr-, and Ba-alloyed MgB_4 simulated using Phono3py.[39,40] Alloying was simulated to 10%. The figure was plotted using ThermoParser.[43]

Mg and the alloyed atom, the greater the reduction in lattice thermal conductivity. Therefore, Ba-alloying up to 10% is shown to result in a reduction in lattice thermal conductivity of up to 58% from 11.6 W m^{-1} K^{-1} in the pure-MgB_4 system to 4.84 W m^{-1} K^{-1} in the alloyed $Mg_{0.9}Ba_{0.1}B_4$ system. Pure Mg_2X compounds have reported lattice thermal conductivities between 6 and 8 W m^{-1} K^{-1} at room temperature, comparably higher than that of the alloyed system reported here.[12]

As a result of this reduction in lattice thermal conductivity and assumed negligible effect on the electronic transport properties, the predicted ZT of this system at the predicted carrier concentration of 1.05×10^{20} cm^{-3} and 1200 K is 0.62, a 32% increase, as depicted in Figure 17.

CONCLUSIONS

We have successfully predicted a new high-performance lightweight thermoelectric material that is stable at high temperatures. By employing hybrid-DFT and lattice dynamics calculations, we have demonstrated that the optimization of MgB_4 through Ba-alloying (10%) has a calculated ZT value of 0.62 at 1200 K and a carrier concentration of 1.05×10^{20} cm^{-3}. These results are comparable to the performance of existing Mg-based systems like $Mg_{3-x}Na_xSb_2$ and Mg_3Sb_2 with experimental ZTs of 0.60 at 773 K and 0.51 at 725 K, respectively, which can be used for lightweight applications.

Moreover, we have outlined design principles that effectively minimize the lattice thermal conductivity while controlling the carrier conductivity. As a result, the introduction of n-type defects would allow for the reduction in hole carrier concentration, moving closer to the optimum predicted value

https://doi.org/10.1021/acs.chemmater.4c00584
Chem. Mater. 2024, 36, 6062−6073

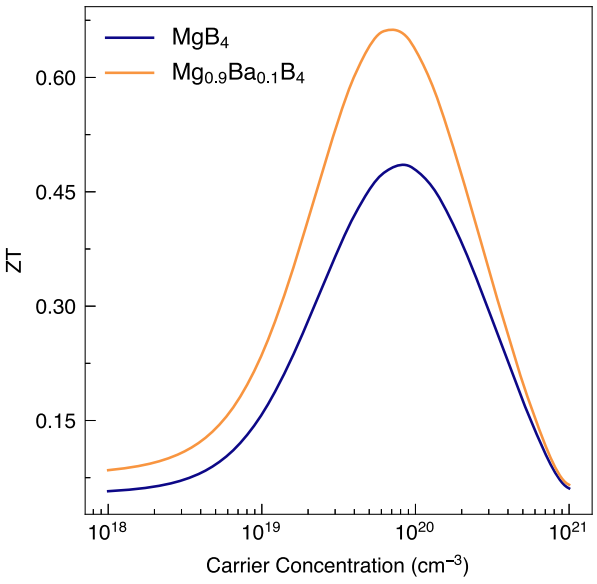

Figure 17. Thermoelectric figure of merit, ZT, of MgB_4 and Ba-alloyed $Mg_{0.9}Ba_{0.1}B_4$ systems at 1200 K. The figure was plotted using ThermoParser.[43]

of 7.50×10^{19} cm^{-3}, and subsequently achieving a ZT value of 0.66.

One advantage of this new material is its lightweight nature and the absence of toxic elements. These features make it suitable for a wide range of applications, especially in scenarios where proximity to people is crucial. Areas such as wearable electronics, medical devices, and portable power generation would benefit from its use.

■ ASSOCIATED CONTENT

Supporting Information

The Supporting Information is available free of charge at https://pubs.acs.org/doi/10.1021/acs.chemmater.4c00584.

Crystal structure, convergence testing, calculated constants for use in AMSET, and n-type transport property results (PDF)

■ AUTHOR INFORMATION

Corresponding Author

David O. Scanlon − *The School of Chemistry, University of Birmingham, Birmingham B15 2TT, U.K.;* orcid.org/0000-0001-9174-8601; Email: d.o.scanlon@bham.ac.uk

Authors

Sabrine Hachmioune − *Department of Chemistry, University College London, London WC1H 0AJ, U.K.; Institute of High Performance Computing, Agency of Science Technology and Research, Singapore 138632, Singapore;* orcid.org/0009-0004-9175-9326

Alex M. Ganose − *Department of Chemistry, Imperial College London, London SW7 2AZ, U.K.;* orcid.org/0000-0002-4486-3321

Michael B. Sullivan − *Institute of High Performance Computing, Agency of Science Technology and Research, Singapore 138632, Singapore*

Complete contact information is available at: https://pubs.acs.org/10.1021/acs.chemmater.4c00584

Notes

The authors declare no competing financial interest.

■ ACKNOWLEDGMENTS

We thank Adair Nicolson and Seán R Kavanagh for useful discussion. We are grateful to the UK Materials and Molecular Modelling Hub for computational resources, which is partially funded by EPSRC (EP/P020194/1 and EP/T022213/1) and to UCL for the provision of the Thomas, Kathleen, and Myriad supercomputers. Via our membership in the UK HEC Materials Chemistry Consortium, which is funded by the UK Engineering and Physical Sciences Research Council (EP/R029431), this work used the ARCHER2 UK National Supercomputing Service (https://www.archer2.ac.uk). This work was supported by the A*STAR Computational Resource Centre through the use of its high-performance computing facilities.

■ REFERENCES

(1) Firth, A.; Zhang, B.; Yang, A. Quantification of global waste heat and its environmental effects. *Appl. Energy* **2019**, *235*, 1314−1334.

(2) Bian, Q. Waste heat: the dominating root cause of current global warming. *Environ. Syst. Res.* **2020**, *9*, 8.

(3) Chen, L.-C.; Chen, P.-Q.; Li, W.-J.; Zhang, Q.; Struzhkin, V. V.; Goncharov, A. F.; Ren, Z.; Chen, X.-J. Enhancement of thermoelectric performance across the topological phase transition in dense lead selenide. *Nat. Mater.* **2019**, *18*, 1321−1326.

(4) Ando Junior, O.; Maran, A.; Henao, N. A review of the development and applications of thermoelectric microgenerators for energy harvesting. *Renewable Sustainable Energy Rev.* **2018**, *91*, 376−393.

(5) Jia, Y.; Jiang, Q.; Sun, H.; Liu, P.; Hu, D.; Pei, Y.; Liu, W.; Crispin, X.; Fabiano, S.; Ma, Y.; Cao, Y. Wearable Thermoelectric Materials and Devices for Self-Powered Electronic Systems. *Adv. Mater.* **2021**, *33*, 2102990.

(6) Tan, G.; Ohta, M.; Kanatzidis, M. G. Thermoelectric power generation: from new materials to devices. *Philos. Trans. R. Soc., A* **2019**, *377*, 20180450.

(7) Hewawasam, L.; Jayasena, A.; Afnan, M.; Ranasinghe, R.; Wijewardane, M. Waste heat recovery from thermo-electric generators (TEGs). *Energy Rep.* **2020**, *6*, 474−479.

(8) Hao, X.; Chen, X.; Zhou, X.; Zhang, L.; Tao, J.; Wang, C.; Wu, T.; Dai, W. Performance Optimization for PbTe-Based Thermoelectric Materials. *Front. Energy Res.* **2021**, *9*, 754532.

(9) Tritt, T. M.; Subramanian, M. A. Thermoelectric Materials, Phenomena, and Applications: A Bird's Eye View. *MRS Bull.* **2006**, *31*, 188−198.

(10) Petsagkourakis, I.; Tybrandt, K.; Crispin, X.; Ohkubo, I.; Satoh, N.; Mori, T. Thermoelectric materials and applications for energy harvesting power generation. *Sci. Technol. Adv. Mater.* **2018**, *19*, 836−862.

(11) Santos, R.; Aminorroaya Yamini, S.; Dou, S. X. Recent progress in magnesium-based thermoelectric materials. *J. Mater. Chem. A* **2018**, *6*, 3328−3341.

(12) Zhou, Z.; Han, G.; Lu, X.; Wang, G.; Zhou, X. High-performance magnesium-based thermoelectric materials: Progress and challenges. *J. Magnesium Alloys* **2022**, *10*, 1719−1736.

(13) Kirkham, M. J.; dos Santos, A. M.; Rawn, C. J.; Lara-Curzio, E.; Sharp, J. W.; Thompson, A. J. Ab initio determination of crystal structures of the thermoelectric material MgAgSb. *Phys. Rev. B: Condens. Matter Mater. Phys.* **2012**, *85*, 144120.

(14) Shuai, J.; Wang, Y.; Kim, H. S.; Liu, Z.; Sun, J.; Chen, S.; Sui, J.; Ren, Z. Thermoelectric properties of Na-doped Zintl compound: Mg3-Na Sb2. *Acta Mater.* **2015**, *93*, 187−193.

(15) Song, L.; Zhang, J.; Iversen, B. B. Simultaneous improvement of power factor and thermal conductivity via Ag doping in p-type

Mg_3Sb_2 thermoelectric materials. *J. Mater. Chem. A* **2017**, *5*, 4932−4939.
(16) Ishiwata, J.; Muralidhar, M.; Inoue, K.; Murakami, M. Effect of MgB4 Addition on the Superconducting Properties of Polycrystalline MgB2. *Phys. Procedia* **2015**, *65*, 69−72.
(17) Esfahani, M. M. D.; Zhu, Q.; Dong, H.; Oganov, A. R.; Wang, S.; Rakitin, M. S.; Zhou, X.-F. Novel magnesium borides and their superconductivity. *Phys. Chem. Chem. Phys.* **2017**, *19*, 14486−14494.
(18) Tan, K.; Tan, K.-Y.; Pah, L.; Shaari, A.; Chen, S. Synthesis of MgB2 from MgB4 through combinatorial solid state reaction routes. *Solid State Sci. Technol.* **2011**, *19*, 15−19.
(19) Heyd, J.; Scuseria, G. E.; Ernzerhof, M. Hybrid functionals based on a screened Coulomb potential. *J. Chem. Phys.* **2003**, *118*, 8207−8215.
(20) Imai, Y.; Mukaida, M.; Ueda, M.; Watanabe, A. Screening of the possible boron-based n-type thermoelectric conversion materials on the basis of the calculated densities of states of metal borides and doped β-boron. *Intermetallics* **2001**, *9*, 721−734.
(21) Momma, K.; Izumi, F. *VESTA* 3for three-dimensional visualization of crystal, volumetric and morphology data. *J. Appl. Crystallogr.* **2011**, *44*, 1272−1276.
(22) Kresse, G.; Hafner, J. Ab initio molecular dynamics for liquid metals. *Phys. Rev. B: Condens. Matter Mater. Phys.* **1993**, *47*, 558−561.
(23) Kresse, G.; Hafner, J. Ab initio molecular-dynamics simulation of the liquid-metal−amorphous-semiconductor transition in germanium. *Phys. Rev. B: Condens. Matter Mater. Phys.* **1994**, *49*, 14251−14269.
(24) Kresse, G.; Furthmüller, J. Efficient iterative schemes for ab initio total-energy calculations using a plane-wave basis set. *Phys. Rev. B: Condens. Matter Mater. Phys.* **1996**, *54*, 11169−11186.
(25) Kresse, G.; Furthmüller, J. Efficiency of ab-initio total energy calculations for metals and semiconductors using a plane-wave basis set. *Comput. Mater. Sci.* **1996**, *6*, 15−50.
(26) Kresse, G.; Joubert, D. From ultrasoft pseudopotentials to the projector augmented-wave method. *Phys. Rev. B: Condens. Matter Mater. Phys.* **1999**, *59*, 1758−1775.
(27) Blöchl, P. E. Projector augmented-wave method. *Phys. Rev. B: Condens. Matter Mater. Phys.* **1994**, *50*, 17953−17979.
(28) Tolba, S. A.; Gameel, K. M.; Ali, B. A.; Almossalami, H. A.; Allam, N. K. *Density Functional Calculations-Recent Progresses of Theory and Application*; InTech, 2018.
(29) Perdew, J. P.; Ruzsinszky, A.; Csonka, G. I.; Vydrov, O. A.; Scuseria, G. E.; Constantin, L. A.; Zhou, X.; Burke, K. Restoring the Density-Gradient Expansion for Exchange in Solids and Surfaces. *Phys. Rev. Lett.* **2008**, *100*, 136406.
(30) Einhorn, M.; Williamson, B. A. D.; Scanlon, D. O. Computational prediction of the thermoelectric performance of LaZnOPn (Pn = P, As). *J. Mater. Chem. A* **2020**, *8*, 7914−7924.
(31) Skelton, J. M.; Burton, L. A.; Parker, S. C.; Walsh, A.; Kim, C.-E.; Soon, A.; Buckeridge, J.; Sokol, A. A.; Catlow, C. R. A.; Togo, A.; Tanaka, I. Anharmonicity in the High-Temperature Cmcm Phase of SnSe: Soft Modes and Three-Phonon Interactions. *Phys. Rev. Lett.* **2016**, *117*, 075502.
(32) Rahim, W.; Skelton, J. M.; Savory, C. N.; Evans, I. R.; Evans, J. S. O.; Walsh, A.; Scanlon, D. O. Polymorph exploration of bismuth stannate using first-principles phonon mode mapping. *Chem. Sci.* **2020**, *11*, 7904−7909.
(33) Birkett, M.; Savory, C. N.; Fioretti, A. N.; Thompson, P.; Muryn, C. A.; Weerakkody, A. D.; Mitrovic, I. Z.; Hall, S.; Treharne, R.; Dhanak, V. R.; Scanlon, D. O.; Zakutayev, A.; Veal, T. D. Atypically small temperature-dependence of the direct band gap in the metastable semiconductor copper nitride Cu_3N. *Phys. Rev. B* **2017**, *95*, 115201.
(34) Mori-Sánchez, P.; Cohen, A. J.; Yang, W. Localization and Delocalization Errors in Density Functional Theory and Implications for Band-Gap Prediction. *Phys. Rev. Lett.* **2008**, *100*, 146401.
(35) Skelton, J. M.; Tiana, D.; Parker, S. C.; Togo, A.; Tanaka, I.; Walsh, A. Influence of the exchange-correlation functional on the quasi-harmonic lattice dynamics of II-VI semiconductors. *J. Chem. Phys.* **2015**, *143*, 064710.
(36) Pulay, P. Ab initio calculation of force constants and equilibrium geometries in polyatomic molecules. *Mol. Phys.* **1969**, *17*, 197−204.
(37) Brlec, K.; Davies, D.; Scanlon, D. Surfaxe: Systematic surface calculations. *J. Open Source Softw.* **2021**, *6*, 3171.
(38) Ganose, A. M.; Park, J.; Faghaninia, A.; Woods-Robinson, R.; Persson, K. A.; Jain, A. Efficient calculation of carrier scattering rates from first principles. *Nat. Commun.* **2021**, *12*, 2222.
(39) Togo, A.; Chaput, L.; Tanaka, I. Distributions of phonon lifetimes in Brillouin zones. *Phys. Rev. B: Condens. Matter Mater. Phys.* **2015**, *91*, 094306.
(40) Togo, A. First-principles Phonon Calculations with Phonopy and Phono3py. *J. Phys. Soc. Jpn.* **2023**, *92*, 012001.
(41) Mizokami, K.; Togo, A.; Tanaka, I. Lattice thermal conductivities of two SiO2 polymorphs by first-principles calculations and the phonon Boltzmann transport equation. *Phys. Rev. B* **2018**, *97*, 224306.
(42) M Ganose, A.; J Jackson, A.; O Scanlon, D. sumo: Command-line tools for plotting and analysis of periodic ab initio calculations. *J. Open Source Softw.* **2018**, *3*, 717.
(43) Spooner, K. B.; Einhorn, M.; Davies, D. W.; Scanlon, D. O. ThermoParser: Streamlined Analysis of Thermoelectric Properties, 2023. https://github.com/SMTG-UCL/ThermoParser (accessed 26 April, 2024).
(44) Hellman, O.; Shulumba, N. Temperature dependent effective potential 1.1, 2018. https://ollehellman.github.io/ (accessed May 04, 2023).
(45) Freysoldt, C.; Grabowski, B.; Hickel, T.; Neugebauer, J.; Kresse, G.; Janotti, A.; Van de Walle, C. G. First-principles calculations for point defects in solids. *Rev. Mod. Phys.* **2014**, *86*, 253−305.
(46) Jain, A.; Ong, S. P.; Hautier, G.; Chen, W.; Richards, W. D.; Dacek, S.; Cholia, S.; Gunter, D.; Skinner, D.; Ceder, G.; Persson, K. A. Commentary: The Materials Project: A materials genome approach to accelerating materials innovation. *APL Mater.* **2013**, *1*, 011002.
(47) Buckeridge, J.; Scanlon, D.; Walsh, A.; Catlow, C. Automated procedure to determine the thermodynamic stability of a material and the range of chemical potentials necessary for its formation relative to competing phases and compounds. *Comput. Phys. Commun.* **2014**, *185*, 330−338.
(48) Kavanagh, S. R. doped, 2023. https://github.com/SMTG-UCL/doped (accessed May 04, 2023).
(49) Mosquera-Lois, I.; Kavanagh, S. R.; Walsh, A.; Scanlon, D. O. ShakeNBreak: Navigating the defect configurational landscape. *J. Open Source Softw.* **2022**, *7*, 4817.
(50) Mosquera-Lois, I.; Kavanagh, S. R. In search of hidden defects. *Matter* **2021**, *4*, 2602−2605.
(51) Mosquera-Lois, I.; Kavanagh, S. R.; Walsh, A.; Scanlon, D. O. Identifying the ground state structures of point defects in solids. *npj Comput. Mater.* **2023**, *9*, 25.
(52) Squires, A. G.; Scanlon, D. O.; Morgan, B. J. py-sc-fermi: self-consistent Fermi energies and defect concentrations from electronic structure calculations. *J. Open Source Softw.* **2023**, *8*, 4962.
(53) Buckeridge, J. Equilibrium point defect and charge carrier concentrations in a material determined through calculation of the self-consistent Fermi energy. *Comput. Phys. Commun.* **2019**, *244*, 329−342.
(54) Sato, Y.; Saito, T.; Tsuchiya, K.; Terauchi, M.; Saito, H.; Takeda, M. Electron energy-loss and soft X-ray emission spectroscopy of electronic structure of MgB4. *J. Solid State Chem.* **2017**, *253*, 58−62.
(55) Yang, X.; Zhao, Y.; Dai, Z.; Zulfiqar, M.; Zhu, J.; Ni, J. Thermal expansion induced reduction of lattice thermal conductivity in light crystals. *Phys. Lett. A* **2017**, *381*, 3514−3518.
(56) Zhang, G.; Xu, C.; Wang, M.; Dong, Y.; Sun, F.; Ren, X.; Xu, H.; Zhao, Y. Pressure Effect of the Mechanical, Electronics and

Thermodynamic Properties of Mg-B Compounds: A First-Principles Investigation. *Sci. Rep.* **2021**, *11*, 6096.
(57) Bradley, C.; Cracknell, A. *The Mathematical Theory of Symmetry in Solids*; Oxford University Press, 2010.
(58) Wang, N.; Li, M.; Xiao, H.; Gao, Z.; Liu, Z.; Zu, X.; Li, S.; Qiao, L. Band degeneracy enhanced thermoelectric performance in layered oxyselenides by first-principles calculations. *npj Comput. Mater.* **2021**, *7*, 18.
(59) Gibbs, Z. M.; Ricci, F.; Li, G.; Zhu, H.; Persson, K.; Ceder, G.; Hautier, G.; Jain, A.; Snyder, G. J. Effective mass and Fermi surface complexity factor from ab initio band structure calculations. *npj Comput. Mater.* **2017**, *3*, 8.
(60) Rawat, P. K.; Paul, B.; Banerji, P. Exploration of Zn Resonance Levels and Thermoelectric Properties in I-Doped PbTe with ZnTe Nanostructures. *ACS Appl. Mater. Interfaces* **2014**, *6*, 3995−4004.
(61) Nishitani, J.; Yu, K. M.; Walukiewicz, W. Charge transfer and mobility enhancement at CdO/SnTe heterointerfaces. *Appl. Phys. Lett.* **2014**, *105*, 132103.
(62) Ganose, A. M. bapt, 2017. https://github.com/utf/bapt (accessed May 04, 2023).
(63) Toberer, E. S.; Zevalkink, A.; Snyder, G. J. Phonon engineering through crystal chemistry. *J. Mater. Chem.* **2011**, *21*, 15843.
(64) Zhang, L.; Li, N.; Wang, H.-Q.; Zhang, Y.; Ren, F.; Liao, X.-X.; Li, Y.-P.; Wang, X.-D.; Huang, Z.; Dai, Y.; Yan, H.; Zheng, J.-C. Tuning the thermal conductivity of strontium titanate through annealing treatments. *Chin. Phys. B* **2017**, *26*, 016602.
(65) Ahmed, A. J.; Nazrul Islam, S. M. K.; Hossain, R.; Kim, J.; Kim, M.; Billah, M.; Hossain, M. S. A.; Yamauchi, Y.; Wang, X. Enhancement of thermoelectric properties of La-doped $SrTiO_3$ bulk by introducing nanoscale porosity. *R. Soc. Open Sci.* **2019**, *6*, 190870.
(66) Freer, R.; Ekren, D.; Ghosh, T.; Biswas, K.; Qiu, P.; Wan, S.; Chen, L.; Han, S.; Fu, C.; Zhu, T.; et al. Key properties of inorganic thermoelectric materials—tables (version 1). *J. Phys.: Energy* **2022**, *4*, 022002.
(67) Wang, H.; Li, J.-F.; Zou, M.; Sui, T. Synthesis and transport property of AgSbTe2 as a promising thermoelectric compound. *Appl. Phys. Lett.* **2008**, *93*, 202106.
(68) Hong, T.; Guo, C.; Wang, D.; Qin, B.; Chang, C.; Gao, X.; Zhao, L.-D. Enhanced thermoelectric performance in SnTe due to the energy filtering effect introduced by Bi2O3. *Mater. Today Energy* **2022**, *25*, 100985.
(69) Pei, Y.; Shi, X.; LaLonde, A.; Wang, H.; Chen, L.; Snyder, G. J. Convergence of electronic bands for high performance bulk thermoelectrics. *Nature* **2011**, *473*, 66−69.
(70) Kim, H.-S.; Heinz, N. A.; Gibbs, Z. M.; Tang, Y.; Kang, S. D.; Snyder, G. J. High thermoelectric performance in (Bi0.25Sb0.75)-2Te3 due to band convergence and improved by carrier concentration control. *Mater. Today* **2017**, *20*, 452−459.
(71) Pfefferle, L.; Fang, F.; Iyyamperumal, E.; Keskar, G. *Nanostructures of Boron, Carbon and Magnesium Diboride for High Temperature Superconductivity*, 2013.

https://doi.org/10.1021/acs.chemmater.4c00584
Chem. Mater. 2024, 36, 6062−6073